Trans-Dimensional Inversion of Modal Dispersion Data on the New England Mud Patch

Julien Bonnel, *Member, IEEE*, Stan E. Dosso, Dimitrios Eleftherakis, and N. Ross Chapman, *Fellow, IEEE*

***Abstract*—This paper presents single receiver geoacoustic inversion of two independent data sets recorded during the 2017 seabed characterization experiment on the New England Mud Patch. In the experimental area, the water depth is around 70 m, and the seabed is characterized by an upper layer of fine grained sediments with clay (i.e., mud). The first data set considered in this paper is a combustive sound source signal, and the second is a chirp emitted by a J15 source. These two data sets provide differing information on the geoacoustic properties of the seabed, as a result of their differing frequency content, and the dispersion properties of the environment. For both data sets, source/receiver range is about 7 km, and modal time-frequency dispersion curves are estimated using warping. Estimated dispersion curves are then used as input data for a Bayesian trans-dimensional inversion algorithm. Subbottom layering and geoacoustic parameters (sound speed and density) are thus inferred from the data. This paper highlights important properties of the mud, consistent with independent *in situ* measurements. It also demonstrates how information content differs for two data sets collected on reciprocal tracks, but with different acoustic sources and modal content.**

***Index Terms*—Geoacoustic inversion, New England mud patch, seabed characterization experiment (SBCEX), underwater acoustics, warping.**

I. Introduction

WHAT is mud? Any child would come with a quick and trivial answer: mud is a brown sticky thing, fun to play with. When asked the same question, an acoustical oceanographer may have to think twice. A muddy sediment is a fined grained sediment with clay content, without any doubt. But what about its specific geoacoustic properties? These are largely unknown, as most historical geoacoustic inversion studies have focused on sandy sites. To learn more about mud, an ocean acoustics experiment—called seabed characterization experiment (SBCEX)—was designed, and took place on the New England Mud Patch, in March/April 2017. The mud patch is a shallow water area (depth $\sim$70 m) with a relatively flat bathymetry, located 110 km south of Cape Cod, MA, USA. The main feature of the seabed is an upper layer of mud [1], [2], which justifies this location as the SBCEX area. Indeed, the main objectives of SBCEX are first, to understand the physical mechanisms that control sound propagation in mud, second, to quantify uncertainties in estimated seabed model parameters, and third, to assess the resulting geoacoustic models and inversion methods. To reach these goals, both *in situ* direct measurements and acoustical remote sensing methods have been deployed. Particular care was taken to cover a wide frequency band, from $\sim$10 Hz to $\sim$50 kHz. This paper focuses on the last two objectives of SBCEX: estimating seabed parameters with uncertainties, and assessing the consistency of inversion methods. The scope of this paper is restricted to low-frequency propagation ($f < 500$ Hz) at intermediate range ($r \sim 7$ km) in a single receiver context.

At the frequencies, ranges, and water depths discussed here, the oceanic environment acts as a dispersive waveguide. Propagation can be described by normal-mode theory, and the pressure field can be modeled by a set of modes that propagates dispersively [3]. Each frequency component of each mode travels with its own group speed, so that modal arrivals have frequency dependent travel times. Provided that these travel times can be estimated from the data, they can be used as input for inversion algorithms, to estimate source range [4]–[7], water sound-speed profile (SSP) [8], [9], and/or seabed geoacoustic properties [5], [9]–[12].

In a single receiver context, a convenient way to resolve the modal travel times is to plot the signal in the time-frequency (TF) domain. The TF positions of the modes are called modal *dispersion curves*: they provide a direct measurement of the frequency dependent travel times, which in turn are related to range and modal group speeds. However, it is well known that modal separability increases with range [3], and one cannot naturally resolve modes in the TF domain except at long ranges [13]. In such case, it is necessary to resort to more advanced signal processing. In the past ten years, a nonlinear processing method called *warping* has emerged as an effective way to resolve modes with a single receiver, even when they are not separated on a conventional spectrogram [5]–[9], [11], [13]–[18].

Modal travel times have been used recently for geoacoustic inversion in the SBCEX context by Wan *et al.* [19] and Bonnel *et al.* [20]. The first study [19] considered a (relatively) long range ($r \sim 15$ km), so that the low-frequency components ($f < 80$ Hz) of the first 4 modes were resolved on conventional

Manuscript received August 27, 2018; revised November 19, 2018; accepted January 22, 2019. Date of publication February 19, 2019; date of current version January 13, 2020. This work was supported in part by the Office of Naval Research and in part by the Office of Naval Research Global. *(Corresponding author: Julien Bonnel.)*

Guest Editor: P. Wilson.

J. Bonnel is with the Department of Applied Ocean Physics and Engineering, Woods Hole Oceanographic Institution, Woods Hole, MA 02543 USA (e-mail: jbonnel@whoi.edu; chapman@uvic.ca).

S. E. Dosso and N. R. Chapman are with the School of Earth and Ocean Sciences, University of Victoria, Victoria, BC V8W 2Y2, Canada (e-mail: sdosso@uvic.ca).

D. Eleftherakis is with the Laboratoire des Sciences et Techniques de l'Information, de la Communication Ecole Nationale Superieure de Techniques Avancees, Brest 29200, France (e-mail: dimitrios.eleftherakis@ensta-bretagne.fr).

Digital Object Identifier 10.1109/JOE.2019.2896389

TF representations. The second study [20] was performed at shorter range ($r \sim 5$ km), and warping was used to resolve up to mode number 18 over the frequency band 20–440 Hz. The two studies were conducted on different tracks, but they consistently indicate that the sound-speed ratio at the mud/water interface is slightly lower than 1, and that a positive strong gradient is required in the mud layer to fit the data (this will be questioned later in this paper). However, neither of these studies quantified uncertainty about the geoacoustic estimates. Also, both studies used a fixed knowledge about the subbottom layering, applying information collected during a chirp reflection survey, carried out before SBCEX. As a result, neither of these studies addressed the fundamental questions about the amount of the seabed structure that can be resolved using modal TF dispersion curves.

The present paper also focuses on geoacoustic inversion of modal TF dispersion curves. However, an emphasis is placed on filling the gaps noted above: assessment of the information content of the data, and uncertainty estimation. To do so, geoacoustic inversion is performed in a Bayesian framework, allowing a quantitative estimation of the uncertainties. Also, model parameterization is inferred from the data, using a trans-dimensional (trans-D) methodology. As a result, geoacoustic parameters (sound speed, density), subbottom layering and associated uncertainties are estimated. Note that a proper estimation of the uncertainty requires knowledge of the data error statistics, which in general are unknown *a priori*. In this paper, data error statistics are also estimated from the data, using a trans-D autoregressive (AR) process to model the error correlation over frequency.

Mode estimation with warping and trans-D inversion is applied to two independent data sets. The source for the first data set is a combustive sound source (CSS) signal, i.e., a powerful wideband impulsive signal [21]. The source for the second data set is a J15-1 towed source, producing low-frequency chirps at relatively low signal-to-noise ratio (SNR). For the two data sets, single hydrophone receptions are considered. The source/receiver configurations are such that the two experimental tracks are reciprocal, i.e., the two tracks are virtually identical, but source and receiver positions are exchanged. This configuration enables verification of the consistency of the inversion results. It also illustrates how data information content varies with source type, and thus with number of modes and bandwidth. Note that trans-D geoacoustic inversion has been successfully applied in the past to modal TF dispersion curves for a hard seabed [9], but this paper is the first in a fine grained sediment context. More importantly, this paper provides new information about inversion consistency and data information content, by using a common method to compare two independent data sets, nearly collocated in space and under similar ocean environment conditions.

The remainder of this paper is organized as follows. Section II briefly describes the SBCEX experiment and the two data sets used in this paper. Sections III and IV successively review the dispersion curve estimation method, and the trans-D inversion method. Section V presents the inversion results for the CSS data set while Section VI presents the results for the J15 data set. Finally, Section VII discusses the result of the two inversions, and provides comparison with the state-of-the-art knowledge of the SBCEX area. Section VIII concludes this paper.

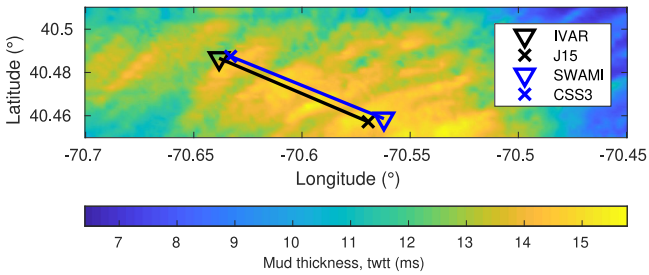

Fig. 1. Map of the mud patch. The background color gives the mud thickness, as measured in twtt. The source locations considered in this paper are shown as crosses, while the receiver locations are shown as triangles.

II. Experiment Description

A. Seabed Characterization Experiment

The SBCEX took place on the New England Mud Patch, 110 km south of Cape Cod, MA, USA, in March/April 2017. This region is characterized by a smooth bathymetry. The main feature of the seabed in the experimental area is a top layer of fine grained sediments (i.e., mud) [1], [2], whose geoacoustic properties were unknown before SBCEX.

The area was surveyed in late summer 2015, before the main experiment in 2017. The 2015 pilot experiment consisted of first, a multibeam sonar survey to measure bathymetry, second, a chirp seismic reflection survey to assess subbottom layering, and third, an extensive effort of physical sampling with sediment cores. Fig. 1 shows the mud thickness over the experimental areas, as measured in two-way travel times (twtt) during the chirp reflection survey [22]. The mud is thickest in the North-West/South-East direction, with twtt constantly larger than 12 ms. This translates into a layer thickness of approximately 9 m, assuming a sound speed of 1500 m/s.

Many acoustic instruments were deployed during SBCEX. These included AUVs, gliders, moored, and towed acoustic sources/receivers, etc. The water column oceanography was monitored during the whole experiment. The winter weather and various storms occurring before and during SBCEX ensured a well mixed water column. As a result, the water SSP was relatively uniform and constant, an ideal situation for geoacoustic inversion.

B. Propagation Track

This paper focuses on low-frequency sound propagation ($f <$ 500 Hz) along the thick mud direction. Two specific data sets are considered, which were recorded on reciprocal linear tracks, as illustrated in Fig. 1. The two tracks are separated by about 500 m. At the track extremities, the distances are 460 m (North-East) and 630 m (South-West).

Along these tracks, the source/receiver range is $\sim$7 km, and the subbottom layering is presented in Fig. 2. It consists of a stack of layers, whose interfaces have been resolved during the reflection survey. The first interface is denoted the mud base; it

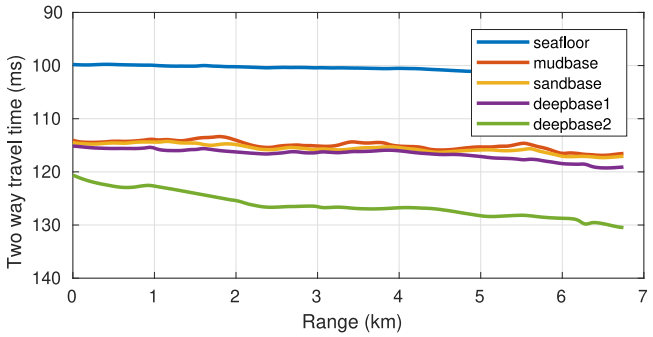

Fig. 2. Subbottom layering along the source/receiver track, based on interpretation of the reflection survey data.

is interpreted to delimit the mud layer that is so characteristic of the SBCEX area. The second interface is interpreted as the base of a sand layer. Both mud and sand have been sampled with cores during the pilot survey, at least in other locations where the mud layer was thinner. The third and fourth interfaces are reflectors delimiting unknown layers, too deep to be sampled by cores. They have been dubbed "deepbase1" and "deepbase2" in the SBCEX jargon. An important feature of the chosen track is that the bathymetry and the subbottom are largely range independent. The only exception is the deepbase2 interface, whose twtt vary by $\sim$10 ms, or $\sim$10 m if one assumes a sound speed of 2000 m/s.

The water SSP was measured on oceanographic moorings in the SBCEX area during the experiment. It is relatively constant and without significant spatial variability. Over the period of interest for this paper, it can be modeled as a constant gradient from 1468 m/s at the surface to 1469 m/s at the seabed.

C. Source and Receiver Specifications

As stated above, this paper focuses on two different source/receiver configurations, which are illustrated in Fig. 1 and described below. In these two cases, water depth can be considered as constant, with $D = 74.5$ m.

1) CSS to SWAMI: The first data set consists of a CSS signal recorded on the shallow water acoustic measurement instrumentation (SWAMI) array. The specific CSS transmission occurred on March 13 around 15:41 UTC at a way-point called "station 3", located at (40.48743 N; 70.632989 W). Three shots were successively emitted at depth $z_s = 20$ m. The specific signal studied in this paper is the first shot of this set. The CSS signal is known to be a high-intensity low-frequency pulse, contaminated by several weaker bubble pulses [21]. The source signature was measured during the experiment using a monitor hydrophone 1 m from the CSS, hard-mounted to the CSS deployment frame. This source signal will be used for source deconvolution, as explained in Section III-B.

The CSS impulsive signal was recorded 6.8 km away on the SWAMI array, located at (40.45865 N; 70.56213 W). The SWAMI is a multihydrophone L-shaped array. A single channel is considered here: hydrophone 10 at depth $z_r = 52$ m. Results on other hydrophones would be expected to be the same, as long as hydrophone depth is not on the null of specific modes.

The time series of the received signal is shown in Fig. 3(a). This figure shows the direct arrival just before $t = 0.1$ s, with a long decaying tail, a classical feature of modal dispersion. The signal also has a precursor 30 ms before the main arrival. This is due to the source signal which produces a small precursor before the main signal, and not to propagation. Overall, the signal has an excellent SNR. Its spectrogram is presented in Fig. 3(b). One can see the same features as in the time series, as well as clearer hints of modal dispersion. This will be discussed further in Sections III and V.

2) J15 to IVAR: The second data set consists of a J15 signal recorded on the intensity vector autonomous recorder (IVAR). The J15 is a towed, low-frequency, acoustic source. The considered J15 signal is a linear chirp from 50 to 250 Hz in 1.6 s. Chirps were emitted every 6 s on March 18 at depth $z_s = 42$ m. The specific signal studied in this paper is a single chirp emitted at 11:01 UTC, located at (40.4572 N; 70.5694 W). The J15 signal was controlled using an analog signal generator. The knowledge of the generated signal will be used for phase compensation, as explained in Section III-B.

The J15 chirp was recorded 6.7 km away on the IVAR, located at (40.48655 N; 70.63831 W). The IVAR is a bottom moored instrument measuring particle motion, as well as sound pressure. Only the sound pressure is considered here, recorded on the IVAR hydrophone, 0.65 m above the seafloor.

The received signal is bandpass filtered between 50 and 250 Hz. The time series of the filtered signal is shown on Fig. 4(a). The chirp starts around $t = 0.1$ s and lasts until $t = 1.7$ s, but the SNR is too low to clearly see the signal. Fig. 4(b) shows the spectrogram of the received signal, where the chirp's shape is clearer. Modal dispersion cannot be visually resolved on this spectrogram. It is nonetheless present in the data, and this will be discussed further in Sections III and VI.

Significant wave height was obtained from the National Data Buoy Center, Station 44097 (Block Island). It is $\simeq$ 1.4 m during the CSS experiment, and $\simeq$ 1.0 m during the J15 experiment. Since our inversion is based on mode travel times and not on signal amplitude, the impact of sea surface roughness is not likely strong. Roughness may scatter the signal and take energy out of the forward field, but the effect on travel time is assumed to be small. From the inversion point of view, it will be included into the unavoidable model mismatch.

III. Dispersion Curve Estimation

A. Modal Propagation in a Single Receiver Context

In our context (shallow water $D < 100$ m, low-frequency $f < 500$ Hz), acoustic propagation is conveniently described using normal-mode theory. Given a broadband source emitting at depth z_s in a range-independent waveguide, the spectral component of the pressure field $Y(f)$ received at depth z_r after propagation over a range r is given by [3]

$$Y(f) \approx QS(f) \sum_{m=1}^{M} \Psi_m(f, z_s)\Psi_m(f, z_r) \frac{e^{(jrk_m(f) - r\beta_m(f))}}{\sqrt{k_m(f)r}} \tag{1}$$

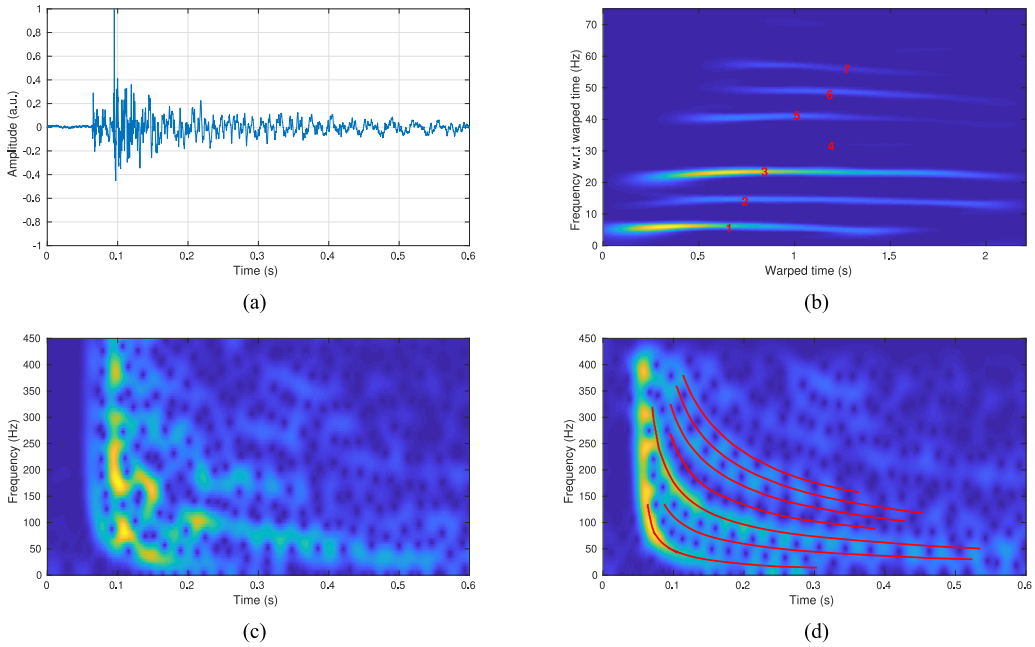

Fig. 3. (a) Received CSS signal (amplitude is normalized and given in arbitrary linear units). (b) Spectrogram of the received signal. (c) Spectrogram of the signal after source deconvolution, and estimated dispersion curves. (d) Spectrogram of the signal after source deconvolution and warping. Modes are labeled in (d) to facilitate understanding. All spectrograms are presented on an arbitrary linear colormap. Note that subfigure layout is counter clockwise from the top left panel.

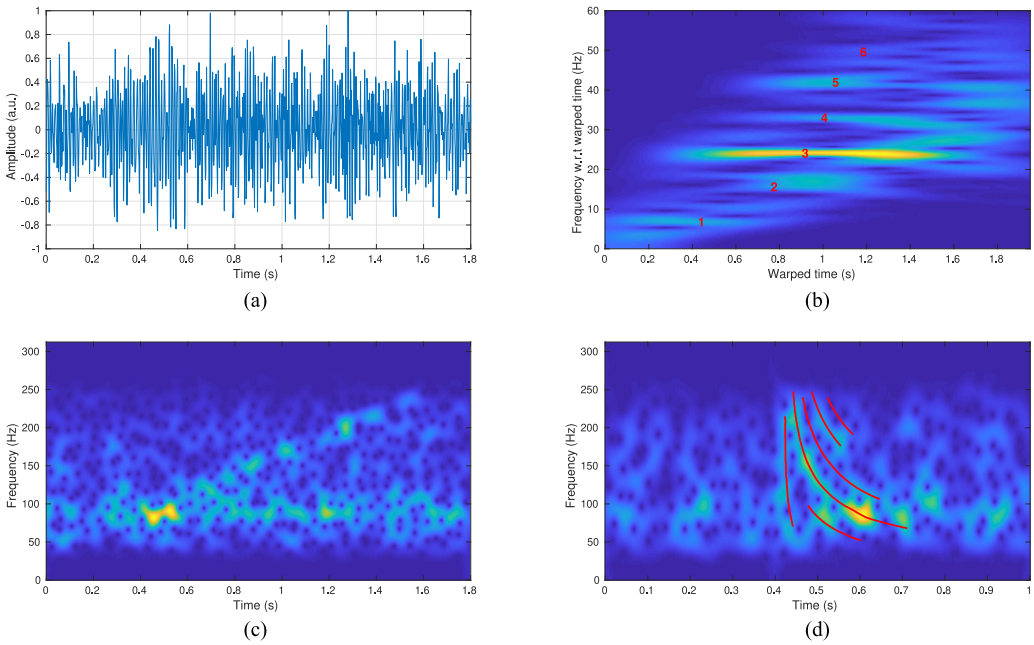

Fig. 4. (a) Received J15 signal (amplitude is normalized and given in arbitrary linear units). (b) Spectrogram of the received signal. (c) Spectrogram of the signal after phase compensation, and estimated dispersion curves. (d) Spectrogram of the signal after source deconvolution and warping. Modes are labeled in (d) to facilitate understanding. All spectrograms are presented on an arbitrary linear colormap. Subfigure layout is the same as in Fig. 3.

where M is the number of propagating modes, and $k_m(f)$, $\beta_m(f)$, and $\Psi_m(f,z)$ are respectively the real part of the horizontal wave number, the imaginary part of the horizontal wave number, and the modal depth function of mode m at frequency f. The term $S(f)$ is the source spectrum, and Q is an unimportant constant factor.

Let us denote $S(f) = |S(f)|e^{j\phi_s(f)}$, with $|S(f)|$ the source amplitude and $\phi_s(f)$ its phase. One can further write (1) more compactly as

$$Y(f) = \sum_{m=1}^{M} A_m(f) e^{j\phi_m(f)} \tag{2}$$

where

$$A_m(f) = Q|S(f)| \frac{\Psi_m(f,z_s)\Psi_m(f,z_r)}{\sqrt{k_m(f)r}} e^{-r\beta_m(f)} \tag{3}$$

is the modal amplitude and

$$\phi_m(f) = \phi_s(f) + k_m(f)r \tag{4}$$

is the mode phase.

As stated in the introduction, in a single receiver context, it is convenient to represent the propagated signal in the TF domain [23]. The TF position of a given mode is defined as its *dispersion curve*. It is given by the mode group delay

$$\tau_m(f) = \frac{1}{2\pi}\frac{d}{df}\left[\phi_m(f)\right] \tag{5a}$$

$$= \tau_s(f) + \frac{r}{v_{gm}(f)} \tag{5b}$$

where $v_{gm}(f) = 2\pi(df/dk_m)$ is the group speed of mode m, and $\tau_s(f) = (1/2\pi)(d/df)\phi_s(f)$ is the source group delay. If the source is an impulse, then $\tau_s(f) = t_s$ is the source emission time. On the other hand, if the source is a frequency modulated chirp, then $\tau_s(f)$ is the inverse function of its instantaneous frequency.

The modal dispersion curves $\tau_m(f)$ depend on the environment through the group speeds $v_{gm}(f)$. They thus depend on seabed layering, sound speeds, and densities. However, seabed attenuation does not impact $v_{gm}(f)$, as its effect is embedded into $\beta_m(f)$, and thus into the mode amplitude $A_m(f)$. As a result, dispersion curves are completely insensitive to seabed attenuation. This paper will thus ignore attenuation, and focus on the other geoacoustic properties. The same holds true for source and receiver depth, which do not impact the group speeds.

The modal dispersion curves also depend on the source intrinsic characteristics, through $\tau_s(f)$. Section III-B will explain how to compensate for the source influence. Two different procedures will be briefly explained: source deconvolution and phase compensation.

B. Source Deconvolution and Phase Compensation

Source deconvolution aims at completely canceling the source influence. The basic idea is to divide $Y(f)$ by $S(f)$, and thus obtain the impulse response of the waveguide. If $S(f)$ is fully known, source deconvolution is straightforward. The only concern is to prevent division by zero (or small values), at frequencies where $S(f)$ is (near) null. Here, a classical deconvolution method is used [24]. The received signal after deconvolution is

$$Y_{\text{deconv}}(f) = \frac{Y(f)S^*(f)}{\max\left\{|S(f)|^2, \epsilon\right\}} \tag{6}$$

with ϵ empirically chosen as $\epsilon = 0.01\max\left\{|S(f)|^2\right\}$.

In our dispersion curve estimation context, only the signal phase is important. In this case, true source deconvolution is not required. One may compensate for the source phase, $\phi_s(f)$, in the following way:

$$Y_{pc}(f) = Y(f)e^{-j\phi_s(f)}. \tag{7}$$

After source deconvolution or phase compensation, the modal phases become

$$\phi_m^{\text{deconv}}(f) = k_m(f)r + 2\pi f dt \tag{8}$$

and the dispersion curves are

$$\tau_m^{\text{deconv}}(f) = \frac{r}{v_{gm}(f)} + dt \tag{9}$$

with dt an unknown time constant that reflects a potential difference between the source and receiver time bases. Note that if source and receiver are synchronized, then $dt = 0$. This is not the case in this paper.

The dispersion curves, as given by (9), do not depend on the source spectrum. They are thus good data to be used as input of geoacoustic inversion algorithms, as only the geoacoustic properties of the seabed need to be inverted for. This will be described in Section IV. Before that, we will recall how a nonlinear processing, called warping, allows high-resolution estimation of the dispersion curves in a single receiver context.

Please note that source deconvolution, as described by (6), has been successfully applied as a preprocessing in warping analysis of another CSS signal recorded during SBCEX [20]. Also, phase compensation, as described by (7), has been successfully applied in warping analysis of baleen whale vocalizations (i.e., low-frequency chirps) recorded in shallow water [6], [16]. In this paper, source deconvolution is applied to the CSS data, while phase compensation is applied to the J15 data.

C. Warping

Generally speaking, warping operates on a given signal $y(t)$ as [25]

$$\mathbf{W}y(t) = \sqrt{|h'(t)|}\,y[h(t)] \tag{10}$$

where $\mathbf{W}y(t)$ is the warped signal and $h(t)$ is the warping function, with $h'(t)$ its time derivative. The warping function $h(t)$ must be bijective. As a result, any warped signal can be unwarped using $h^{-1}(t)$ as the new warping function.

Warping can be adapted to a given physical situation by choosing the suitable $h(t)$. Dispersion based warping has been introduced by Touze *et al.* [14]. Its objective is to transform the signal to increase the separability of the modes by linearizing the modal phase. As a result, warped modes are continuous tones, and thus horizontal in the TF domain. To do so, dispersion-based warping is based on equations approximating the environment by an ideal range-independent waveguide with a perfectly reflecting surface, a constant water sound speed c_w, and a perfectly rigid seabed. In this case, the warping function is

$$h(t) = \sqrt{t^2 + t_r^2} \tag{11}$$

with $t_r = r/c_w$.

Warping has been successfully applied in the past for modal filtering in a variety of scenarios [6], [7], [11], [16], [26], [27]. It has notably been used for geoacoustic/tomographic inversion using CSS [20] and J15 chirp data [8].

D. Dispersion Curve Estimation

After source deconvolution (or phase compensation) and warping, dispersion curve estimation is trivial. The whole process is as follows:

1) perform source deconvolution using (6) or phase compensation using (7), based on prior knowledge of source characteristics;
2) warp the signal using (10) and (11);
3) compute the spectrogram of the warped signal, and filter the (warped) modes using classical TF filtering;
4) unwarp the filtered modes;
5) estimate the group delay (or the instantaneous frequency) of each individual mode.

This process has been used in the warping reference previously cited (see [6]–[8], [11], [16], [20], [26], [27]), and will thus not be detailed here. The reader unfamiliar with it may find detailed explanations in [13]. It is nonetheless interesting to remind that warping requires an accurate determination of the first sample to be warped. This has been recently discussed in [28], and today the best solution seems to be a trial and error process. Doing it well notably improves the dispersion curve estimation of the first mode [28].

Once dispersion curves are estimated, they can be used as input data for geoacoustic inversion algorithms. Section IV details the inverse theory and algorithms used in this paper.

IV. Inverse Theory and Algorithms

This paper uses Bayesian trans-D inversion, which will be quickly reviewed below. More complete treatments of Bayesian methods and/or Markov-chain Monte Carlo methods are given in [29], and applications in geoacoustic inversion can be found in [30].

A. Trans-D Bayesian Inversion

Trans-D inversion is designed to sample probabilistically over a set of possible models that may vary in their number of parameters (dimensions). For example in this paper, models vary in the number of seabed layer interfaces and the order of an AR error model. To describe the approach more generally, consider a finite set $\mathcal{K}$, indexed by k, specifying choices of model parameterizations with the corresponding sets of model parameters denoted as $\mathbf{m}_k$, and let $\mathbf{d}$ represent observed data (modal dispersion curves in this paper). Bayes' theorem for a trans-D model can be written as [29]–[31]

$$P(k,\mathbf{m}_k|\mathbf{d}) = \frac{P(k)\,P(\mathbf{m}_k|k)\,P(\mathbf{d}|k,\mathbf{m}_k)}{\sum_{k'\in\mathcal{K}}\int_{\mathcal{M}_{k'}} P(k')\,P(\mathbf{m}'_{k'}|k')\,P(\mathbf{d}|k',\mathbf{m}'_{k'})\,d\mathbf{m}'_{k'}} \tag{12}$$

where $\mathcal{M}_k$ represents the parameter space associated with index k. In (12), $P(k)P(\mathbf{m}_k|k)$ is the prior probability of the state $(k,\mathbf{m}_k)$, and $P(\mathbf{d}|k,\mathbf{m}_k)$ is the conditional probability of $\mathbf{d}$ given $(k,\mathbf{m}_k)$, which is interpreted as the likelihood of $(k,\mathbf{m}_k)$, denoted as $\mathcal{L}(k,\mathbf{m}_k)$. The posterior probability density (PPD) $P(k,\mathbf{m}_k|\mathbf{d})$ is defined over the trans-D parameter space and quantifies the information content of the data and before constrain the model parameters. The denominator (normalization) on the right side of (12) represents the total Bayesian evidence of the set of possible models.

Markov-chain Monte Carlo methods can be applied to sample the trans-D PPD in (12) to provide marginal probability densities and other statistical measures quantifying parameter uncertainties. The sampling algorithm must transition between models with differing numbers of parameters while satisfying reversibility (detailed balance). The reversible-jump Markov-chain Monte Carlo (rjMCMC) algorithm accomplishes this by accepting a new state $(k',\mathbf{m}'_{k'})$, given a current state $(k,\mathbf{m}_k)$, with probability given by the Metropolis–Hastings–Green criterion [29]

$$A(k',\mathbf{m}'_{k'}|k,\mathbf{m}_k) = \min\left[1,\frac{Q(k,\mathbf{m}_k|k',\mathbf{m}'_{k'})}{Q(k',\mathbf{m}'_{k'}|k,\mathbf{m}_k)}\,\frac{P(k')P(\mathbf{m}'_{k'}|k')}{P(k)\,P(\mathbf{m}_k|k)}\,\frac{\mathcal{L}(k',\mathbf{m}'_{k'})}{\mathcal{L}(k,\mathbf{m}_k)}\,|\mathbf{J}|\right]. \tag{13}$$

In (13), $Q(k',\mathbf{m}'_{k'}|k,\mathbf{m}_k)$ is the proposal probability density of proposing a new state $(k',\mathbf{m}'_{k'})$ given the current state $(k,\mathbf{m}_k)$, and $|\mathbf{J}|$ is the determinant of the Jacobian matrix for the coordinate transformation between parameter subspaces. The most common form of rjMCMC in geophysical inversion adds and deletes parameters (referred to as birth and death steps, respectively) in such a manner that $|\mathbf{J}|=1$. In addition to birth and death steps, rjMCMC applies perturbation steps where parameters of the current model are perturbed randomly without changing model dimension. For geoacoustic parameters with uniform bounded priors, a partition model for interface depths, a symmetric proposal density for perturbation steps, and new parameters in birth steps drawn from the prior, the acceptance criterion for all steps reduces to the likelihood ratio [32]

$$A(k',\mathbf{m}'_{k'}|k,\mathbf{m}_k) = \min\left[1,\frac{\mathcal{L}(k',\mathbf{m}'_{k'})}{\mathcal{L}(k,\mathbf{m}_k)}\right]. \tag{14}$$

Employing effective proposals densities is key to an efficient rjMCMC sampling algorithm. In the approach used here, an efficient proposal density for parameter perturbations is based on principal-component (PC) decomposition of the unit-lag parameter covariance matrix; that is, the covariance estimated from successive parameter changes along the Markov chain [32], [33]. The PC decomposition provides both directions and length scales for effective parameter updates. Perturbations are applied in a rotated parameter space where the axes align with the dominant correlation directions (i.e., PC parameters are uncorrelated). The PC proposal is initiated from an analytic linearized estimate that is subsequently updated with a nonlinear estimate from the on-going sampling (a diminishing adaptation). The acceptance rate of perturbations and birth/death steps is improved by applying the method of parallel tempering (PT) [34], [35], which is based on a series of interacting Markov chains with successively tempered (relaxed) likelihoods raised to powers ≤ 1. PT is also (and mainly) used for escaping local modes in nonlinear MCMC inversions; it ensures the full

posterior is properly sampled. In our case, the PC proposals are adapted individually to the tempering of each Markov chain. This combination of PC proposals and PT has been shown to significantly improve sampling efficiency in trans-D inversion [32], [36].

B. Likelihood Function and AR Error Model

Defining the likelihood function requires specifying the statistical distribution of the data errors, which is then interpreted as a function of the model parameters. In many practical inverse problems the data error distribution, accounting for both measurement and theory/modeling errors, is not well known *a priori*. In such cases, it is reasonable to make a conservative choice, such as a multivariate Gaussian distribution (supported by the Central Limit Theorem and maximum entropy), and consider the parameters of this distribution as unknowns in the inversion. The validity of this choice can be considered *a posteriori* by examining the data residuals (difference between measured and predicted data), which should approximately follow the assumed error distribution.

The measured data considered in this paper consist of a set of dispersion curves $\mathbf{d} = \left[\mathbf{d}_1^T, \mathbf{d}_2^T, \ldots, \mathbf{d}_M^T\right]^T$ for M acoustic modes, with observations at N_i frequencies for the ith mode (i.e., $\mathbf{d}_i$ is a column vector with N_i elements, and the total data set $\mathbf{d}$ includes $N = \sum_{i=1}^{M} N_i$ data). Assuming the data errors are unbiased and Gaussian distributed with independent errors between modes, the likelihood function can be written as

$$\mathcal{L}(\mathbf{m}) = \prod_{i=1}^{M} \frac{1}{(2\pi)^{N_i/2}|\mathbf{C}_{\mathbf{d}i}|^{1/2}} \exp\left[-\mathbf{r}_i(\mathbf{m})^T \mathbf{C}_{\mathbf{d}_i}^{-1} \mathbf{r}_i(\mathbf{m})/2\right] \tag{15}$$

where $\mathbf{r}_i(\mathbf{m}) = \mathbf{d}_i - \mathbf{d}_i(\mathbf{m})$ and $\mathbf{C}_{\mathbf{d}\,i}$ are the data residuals and data error covariance matrix for the ith mode, respectively, with $\mathbf{d}_i(\mathbf{m})$ representing predicted data computed for model parameters $\mathbf{m}$ (the subscript on $\mathbf{m}$ indicating model dimension is not required here and is dropped for simplicity).

We further assume that the error standard deviation for all frequencies of the ith mode is σ_i (i.e., each mode has a distinct standard deviation), and that the error correlation over frequency for the ith mode can be represented by either a zeroth-order or a first-order AR process, denoted as AR(0) and AR(1), respectively. An AR(0) process represents uncorrelated residuals while an AR(1) process represents correlated residuals corresponding to a Toeplitz covariance matrix that decays exponentially away from the main diagonal. It is possible to invert for the parameters of such a covariance matrix. However, the AR error model used here provides a convenient formulation that avoids the requirement to compute the determinant and inverse of the covariance matrix at each sampling step. Furthermore, AR sampling is carried out trans-dimensionally so that the data determine to what extent an AR(0) or AR(1) model is required, to avoid over- or under-parameterizing the error model.

Under the above assumptions, the residual error model accounting for covariance, referred to as the total residuals, can be written as [37], [38]

$$r_{ij}^{(t)}(\mathbf{m}, a_i) = \begin{cases} d_{ij} - d_{ij}(\mathbf{m}), & j = 1 \\ d_{ij} - d_{ij}(\mathbf{m}) + a_i \left[d_{i(j-1)} - d_{i(j-1)}(\mathbf{m})\right], & j = 2, \ldots, N_i \end{cases} \tag{16}$$

where $a_i = 0$ for an AR(0) error process and $a_i \neq 0$ for an AR(1) process. The likelihood can then be written as

$$\mathcal{L}(\mathbf{m}, \mathbf{a}, \boldsymbol{\sigma}) = \prod_{i=1}^{M} \frac{1}{(2\pi\sigma_i^2)^{N_i/2}} \exp\left[-\left|\mathbf{r}_i^{(t)}(\mathbf{m}, \mathbf{a})\right|^2 \Big/ (2\sigma_i^2)\right] \tag{17}$$

where $\mathbf{a} = [a_1, \ldots, a_M]^T$ and $\boldsymbol{\sigma} = [\sigma_1, \ldots, \sigma_M]^T$. In (17) the standard deviations, order (zero or first) of the AR process, and AR(1) coefficients can be treated as unknowns, sampled in the inversion as follows.

A maximum-likelihood estimate for σ_l can be derived by setting $\partial L(\mathbf{m}, \mathbf{a}, \boldsymbol{\sigma})/\partial\sigma_l = 0$, leading to [39], [40]

$$\hat{\sigma}_l(\mathbf{m}, a_l) = \left[\frac{1}{N_l}\left|\mathbf{r}_l^{(t)}(\mathbf{m}, a_l)\right|^2\right]^{1/2}. \tag{18}$$

Substituting (18) back into (17) leads to

$$\mathcal{L}(\mathbf{m}, \mathbf{a}) = \prod_{i=1}^{M} \frac{\exp(-N_i/2)}{(2\pi)^{N_i/2}} \left|\mathbf{r}_i^{(t)}(\mathbf{m}, a_i)\right|^{-N_i}. \tag{19}$$

Equation (19) applies the maximum-likelihood estimate for $\boldsymbol{\sigma}$ in terms of $\mathbf{m}$ and $\mathbf{a}$, such that sampling over $\mathbf{m}$ and $\mathbf{a}$ samples implicitly over the corresponding maximum-likelihood values $\hat{\boldsymbol{\sigma}}(\mathbf{m}, \mathbf{a})$ (i.e., maximum-likelihood standard deviations are automatically applied for each choice of $(\mathbf{m}, \mathbf{a})$) [40].

To consider possible moves in trans-D AR sampling, it is convenient to define a simple notation whereby $\mathbf{m}_0$ represents a model with an AR(0) error process for the ith mode, and $\mathbf{m}_1$ and $\mathbf{m}_1'$ represent models that are identical to $\mathbf{m}_0$ except for an AR(1) error process for the ith mode with values of the AR(1) coefficient of a_i and a_i', respectively. A model with an AR(0) error process has only one move available: a birth step to an AR(1) process. If the proposed AR(1) coefficient in this birth step is drawn from a uniform prior of width Δa, then the proposal density is given by $Q(\mathbf{m}_1|\mathbf{m}_0) = 1/\Delta a$. A model with an AR(1) process has two moves available with equal probability: a death step to an AR(0) process with $Q(\mathbf{m}_0|\mathbf{m}_1) =$ 1/2, and perturbation of the AR(1) parameter with the proposal taken to be $Q(\mathbf{m}_1'|\mathbf{m}_1) = G(a_1'|a_1)/2$, where $G(a_1'|a_1)$ is the value at a_1' of a Gaussian density centered at a_1. With these definitions the acceptance probability of a birth step can be

TABLE I
INVERSION PARAMETER LIST

Parameter	Unit	Search bounds
Number of interfaces k	-	[1 ; 8]
AR coefficient a_m	-	[-0.5 ; 0.99]
Interface depth z_i	m	[0.1 ; 50]
Layer sound speed c_i	m/s	[1440 ; 2500]
Layer density ρ_i	g/cm^3	[1.3 ; 2.4]
Basement sound speed c_b	m/s	[1440 ; 2500]
Basement density ρ_b	g/cm^3	[1.3 ; 2.4]
Range r	km	[6.55 ; 6.95]
Time shift dt	s	[-0.01 ; 0.2]

Prior information is uniform over the given search bound.

determined as [38]

$$A(\mathbf{m}_1|\mathbf{m}_0) = \min\left[1, \frac{Q(\mathbf{m}_0|\mathbf{m}_1)}{Q(\mathbf{m}_1|\mathbf{m}_0)}\frac{P(\mathbf{m}_1)}{P(\mathbf{m}_0)}\frac{\mathcal{L}(\mathbf{m}_1)}{\mathcal{L}(\mathbf{m}_0)}\right] \quad (20)$$

$$= \min\left[1, \frac{1/2}{1/\Delta a}\frac{1/\Delta a}{1}\frac{\mathcal{L}(\mathbf{m}_1)}{\mathcal{L}(\mathbf{m}_0)}\right] \quad (21)$$

$$= \min\left[1, \frac{1}{2}\frac{\mathcal{L}(\mathbf{m}_1)}{\mathcal{L}(\mathbf{m}_0)}\right]. \quad (22)$$

Similarly, the acceptance probabilities of AR death and perturbation moves, respectively, can be shown to be

$$A(\mathbf{m}_0|\mathbf{m}_1) = \min\left[1, 2\frac{\mathcal{L}(\mathbf{m}_1)}{\mathcal{L}(\mathbf{m}_0)}\right] \quad (23)$$

$$A(\mathbf{m}_1'|\mathbf{m}_1) = \min\left[1, \frac{\mathcal{L}(\mathbf{m}_1')}{\mathcal{L}(\mathbf{m}_1)}\right]. \quad (24)$$

C. Summary and Application to SBCEX Data Set

In this paper, the environment is modeled as a range-independent waveguide. Water depth is $D = 74.5$ m. The water SSP is a gradient linear with 1468 m/s at the surface and 1469 m/s at the bottom. The seabed is assumed to be a stack of isospeed layers. The layer sound speeds, densities, and the interface depths are collected into a parameter vector $\mathbf{m}$. As explained before, the size of $\mathbf{m}$ depends on the number of interfaces (and thus layers) of the considered model, as determined by the trans-D method. Also, the inversion samples trans-dimensionally over $\mathbf{a}$, the AR process parameter for each mode covariance.

The data $\mathbf{d}$ is a set of modal dispersion curves. The replicas $\mathbf{d}_i(\mathbf{m})$ are given by (9). They are simulated using the modal code ORCA [41]. Please note that time shift dt and range r are unknown parameters that must be estimated. They are thus included in $\mathbf{m}$.

A uniform prior is set for every parameter. The parameter list and the search bounds are summarized in Table I. The first parameter k is the number of interfaces. The second parameter a_m is the AR coefficient for mode m. Both k and every a_m are sampled trans-dimensionally; their value thus impact the size of the parameter space. The three parameters interface depth z_i, sound speed c_i, and density ρ_i are given for layer i, with $i \in [\![1\,;\,k]\!]$. The four last parameters are c_b, ρ_b, r, and dt; they are not sampled trans-dimensionally. Overall, the size of the parameter space is $3k + 5 + n_a$, with n_a the number of modes whose data error is correlated. Note that the upper limit of 8 for k has been chosen so that the normal mode model would be stable. Also, the upper limit of 50 m for interface depth has been chosen as a compromise between inversion efficiency and the data capacity to resolve deep details. Indeed, one can show with simulation that at the lowest frequency (15 Hz), more than 95% of the mode energy that is in the seabed is above this 50 m limit. We thus assume that our multimode data are essentially insensitive to structure at deeper depths.

For each layer, sound speed and density are related through a two-dimensional (2-D) prior based on Hamilton's empirical relationship [42]. For a given layer i, the algorithm checks if the sound speed c_i and density ρ_i verify $c_{\min} < c_i < c_{\max}$, with

$$c_{\min} = (1.54 - 0.907\rho_i + 0.3695\rho_i^{1.88}) * 1500.4 \quad (25)$$

$$c_{\max} = (1.60 - 0.907\rho_i + 0.3695\rho_i^{2.01}) * 1501.4 \quad (26)$$

with $c_{\min}$ and $c_{\max}$ in meter per second and ρ_i in gram per cubic centimeter. If this relationship is not respected, the model is rejected. This approach defines the Hamilton prior as a uniform probability density over the 2-D $c - \rho$ region within the bounds specified in (25) and (26), with a value of zero outside of this bounded region.

Last but not least, PT is carried out using eight parallel rjMCMC chains. The chains' temperatures are given by a geometric series starting at $T_0 = 1$, and with a constant ratio of 1.3 between successive terms ($T_i = 1.3\,T_{i-1}$). The results presented below are from 2.1×10^4 samples at $T_0 = 1$ after thinning the chain by a factor of 10 and removing the first 10^4 samples as burn-in. The samples presented here thus represent $1/10$th of the samples drawn on the first chain after burn-in, or $1/80$th of the total samples drawn.

V. CSS DATA ANALYSIS

This section presents the CSS data analysis: first, the dispersion curve estimation, and then, the inversion results.

A. Dispersion Curve Estimation

As stated in Section III, the first step for the estimating dispersion curves is source deconvolution, or phase compensation. CSS data are processed with source deconvolution. Indeed, the impulsive nature of the signal is not favorable for defining the source phase, and thus deconvolution is preferred over phase compensation. The spectrogram of the signal after deconvolution is shown in Fig. 3(c). One can note a clear improvement over the raw signal shown in Fig. 3(b). The precursor before the main arrival has disappeared, and the dispersion pattern becomes clearer. Indeed, the raw signal shows interferences between the

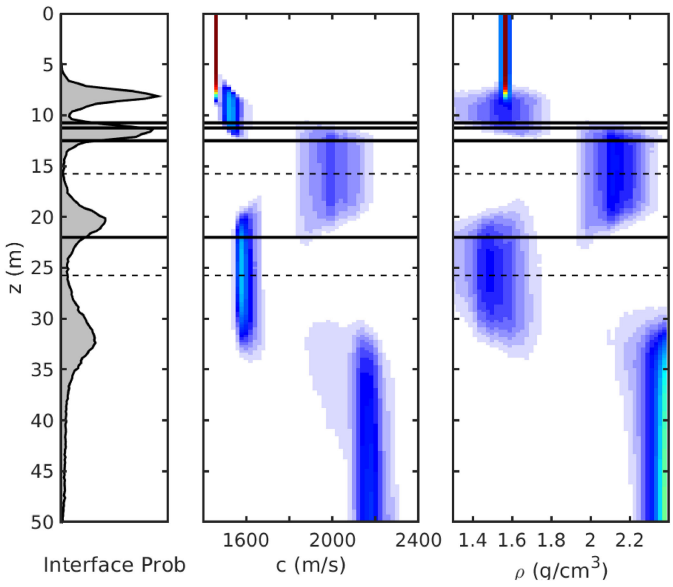

Fig. 5. Trans-D marginal posterior probability profiles for the CSS source signal. The probabilities for the geoacoustic parameter profiles are normalized globally for seabed depth from 0 to 50 m. Averaged interface depths estimated from the reflection survey are plotted as horizontal continuous black lines over the marginal probability densities. Minimum and maximum depths for the lowest horizon (deepbase2) are plotted as horizontal dashed black lines.

main CSS pulse, and secondary arrivals due to the bubble pulses. These are clearly reduced by source deconvolution.

One may wonder about the quality of the source signal recorded on the monitor hydrophone, and used for deconvolution. It obviously cannot be perfectly representative of the true source signal $S(f)$, as it is very likely contaminated by surface and/or ship hull reflection(s). However, the deconvolution result appears to be a significant improvement. It is at least good enough to separate modes with warping. This is illustrated on Fig. 3(d), which shows the spectrogram of the signal after deconvolution and warping. One can see that the modes are clearly separated, and can thus be filtered using conventional TF filtering. Dispersion curves can subsequently be estimated. Successful estimates have been obtained for modes 1 to 7, and for frequencies from 15 to 300 Hz. Estimated dispersion curves are superimposed on the spectrogram in Fig. 3(c).

Note that mode 4 appears absent in Fig. 3(d) while its estimated dispersion curve is present is Fig. 3(c). Actually, mode 4 is visible on the spectrogram of the warped signal, if plotted on a decibel scale. However, this representation obscures the other modes, and is not shown here. The weak excitation of mode 4 is likely due to source and/or receiver depth near a null for this mode.

B. Inversion Results

The estimated dispersion curves shown in Fig. 3(c) serve as input data for the Bayesian trans-D method described in Section IV. Inversion results can be summarized by marginal posterior probability profiles, as shown in Fig. 5, where warmer colors indicate regions of higher probability and white is zero. The averaged depth of the interfaces measured during the reflection survey (and illustrated in Fig. 2) are superimposed on Fig. 5 to facilitate comparison. The minimum and maximum depths of the lowest horizon are also superimposed on Fig. 5. To plot these, the survey twtt (see Fig. 2) have been converted to depth using the cumulative velocities estimated by the inversion. Once again, please note that the inversion results are completely independent from the seabed layering information obtained during the reflection survey (black horizontal lines).

One can see from the left panel of Fig. 5 that the data have information to resolve at least four interfaces. Their most probable depths are $z = 8.1$, 11.3, 20.1, and $\sim$32 m. Please note that this does not preclude the existence of models with more than four interfaces, and/or interfaces at other depths. However, it does say that these four interfaces are consistently present in most sampled models, and hence emerge in the marginalization.

Looking at the two right panels of Fig. 5, one see that the environment very likely has a first isospeed layer with sound speed $c = 1471$ m/s, density $\rho = 1.56$ g/cm^3 and a thickness of about 8 m. After that and during the next 3 m, sound speed increases, with probable values between 1500 and 1600 m/s. This result may actually reflect a sound-speed gradient in this region, from $z \sim 8$ to $z \sim 11$ m. Results at greater depths are more uncertain, although the inversion seems to resolve several deeper layers. The results notably show a low velocity ($\sim$1600 m/s), low density ($\sim$1.5 g/cm^3) layer at depths between about 20–32 m. Such a low density layer below a higher density, apparently consolidated layer is unusual, and may represent an inversion artifact. Inversions sometimes produce unrealistic structure, particularly at greater depths where sensitivities are lower, in an attempt to fit noisy data which may include theory errors that do not exactly follow the inversion assumptions. Particular care has been taken here to model errors, including the trans-D AR processes to represent error correlations and *a posteriori* residual analysis (see Section V-C). Nonetheless, fully characterizing error statistics is a challenging problem, which can lead to spurious model structure. However, it is interesting to note that the velocity and density values between about 20–32 m in Fig. 5 are similar to those at the base of the mud layer at $\sim$12 m depth, such that low velocity/density layer could represent similar sediments, with the higher velocity/density from 12–20 m representing an intervening layer of different composition. Furthermore, a similar low velocity, low density layer was estimated in a previous study, using modal dispersion inversion on another part of the mud patch [20]. Hence, a definitive conclusion on the authenticity of the low velocity/density layer is not possible without deep coring. However, it would be interesting to compare this result with inversions that take into account the mode Airy phase of low order modes (e.g., [19]). Indeed, both Airy phase and the high order modes that are used here are sensitive to features deep below the seabed. In a given frequency band, the consistency of inversion using Airy phase (of low order modes) and/or high order modes is still an open question.

A comparison with the reflection survey shows that the first interface from the inversion at $z \sim 8$ m is well within the mud layer. The interpretation here is that the mud is homogeneous over the first 8 m, and below this is a region with increasing sound speed, likely due to increasing sand content within the

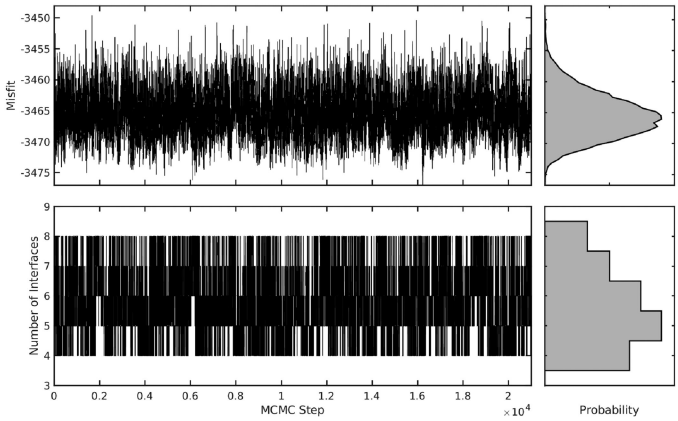

Fig. 6. Sampling history and distribution of the number of interfaces and likelihood values.

mud, before transitioning to sand. The sand layer, resolved by the high-frequency reflection survey, is too thin ($\sim$50 cm) to be resolved by our data set, which has a smallest wavelength of about 3 m. As a result, high speed mud and sand are seen as one by our inversion. Interestingly, the inversion interface at the bottom of the mud/sand coincides closely with the reflection survey sandbase. Deeper, the deepbase1 interface seen by the reflection survey is invisible to our inversion. This once again may be explained by the limited frequency band of our source, preventing resolution of thin layers. However, the inversion resolves an interface around $z = 20$ m, which is generally consistent with the survey deepbase2, particularly given that this interface is range dependent. It also resolves an extra interface around $z = 32$ m, which is too deep to have been seen during the reflection survey.

C. Inversion Quality Check

One must not trust inversion results without checking inversion convergence. To do so, Fig. 6 shows the sampling history of the rjMCMC algorithm. It presents the evolution of the misfit and of the number of interfaces, as well as their distribution. One can see that sampling seems stationary and that misfit distribution is smooth. These, combined with the smooth marginal profiles of Fig. 5, are good indications that the trans-PPD is not under-sampled. Also, marginal profiles from the first half of the sample to those of the second half have been visually compared, and do not show any significant differences. It is thus reasonable to assume convergence.

Interestingly, the number of interface distribution (see Fig. 5) shows that all the sampled models have between four and eight interfaces. This is fully consistent with the four-interface hypothesis stated above. Indeed, extra interfaces are required to create a gradual sound speed increase, as seems to be the case at the base of the mud layer.

It is also important to verify the statistical hypotheses used to define the likelihood function. The assumption of Gaussian-distributed residual errors with correlations described by an AR(0) or AR(1) process is considered in Fig. 7. This figure presents histograms of total residuals (16), and compares them to a Gaussian distribution. The Gaussian hypothesis seems reasonably valid for most modes, but not for all, such as mode four which is clearly bimodal. Fig. 7 also presents autocorrelation of total residuals, and compares these with autocorrelation of raw residuals. The latter have wide central peaks, representative of a strong correlations. However, the autocorrelations of the total residuals have narrow peaks, typically only one point wide. This illustrates that the (total) residuals of all modes are largely uncorrelated (when covariance is taken into account through the trans-D AR process). This ensemble residual analysis generally supports our initial statistical hypothesis about the data error, even if Gaussian hypothesis is not valid for all modes.

VI. J15 Data Analysis

A. Dispersion Curve Estimation

As for the CSS, the first step to estimating dispersion curves is to compensate for the source influence. For the J15 signal, this is done using phase compensation, as explained in Section III-B. Note that source deconvolution has also been tried, and provided similar result. Phase compensation is preferred here because it is a simpler process. Also, it is worth demonstrating that the inversion process does not require a full characterization of the source signal, as phase compensation ignores amplitude information.

The spectrogram after phase compensation is shown in Fig. 4(c). Obviously, phase compensation does not improve SNR. However, one can now see a modal dispersion pattern emerging from the noise. The phase-compensated signal is then warped, and the spectrogram of the warped signal is shown in Fig. 4(d), where modes are labeled in red to facilitate reading. Because of the low SNR, mode identification is relatively difficult in Fig. 4(d). Modal filtering was performed as a trial and error process. The filtering quality was visually assessed by plotting the dispersion curves of the filtered modes on the original spectrogram. The final result is shown on Fig. 4(c). Dispersion curves have been estimated for modes 1 to 6, and for frequencies from 52 to 248 Hz.

B. Inversion Results

As for the CSS, estimated dispersion curves serve as input for the Bayesian trans-D algorithm, and results are summarized by marginal posterior probability profiles, as shown in Fig. 8.

In this case the data do not have sufficient information content to resolve more than one interface, with a most probable depth of $z = 9.1$ m. Above that interface, sound speed and density are very well resolved. Their most probable values are $c = 1474$ m/s and $\rho = 1.56$ g/cm^3. Below this layer is a higher speed/higher density basement, whose geoacoustic properties are less certain. Nonetheless, its sound-speed value (around $c = 2000$ m/s) is a good average of the layered model found by the CSS.

It is particularly interesting to note that the first layer estimated here is thinner than the mud layer, as defined by the reflection survey. However, it is fully consistent with the CSS inversion result, and corresponds to the upper part of the mud which is isospeed. The J15 inversion shows a strong change of

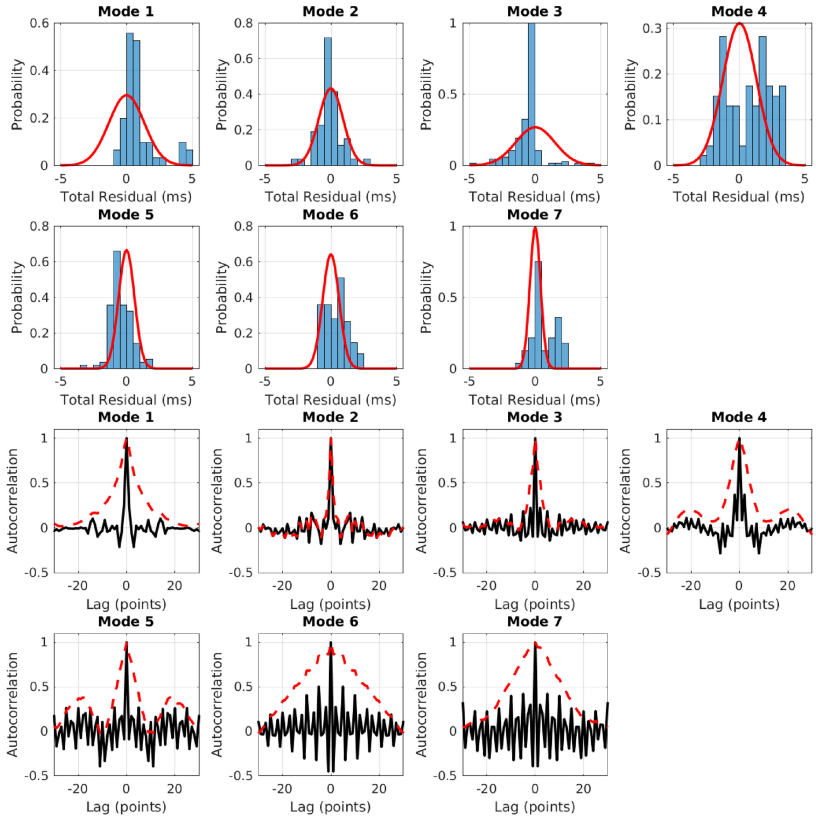

Fig. 7. Posterior ensemble residual analysis. The upper two rows show histograms of total data residuals compared to Gaussian distributions. The lower two rows show compare raw residual autocorrelations (red dashed lines) and total residual autocorrelations (black lines).

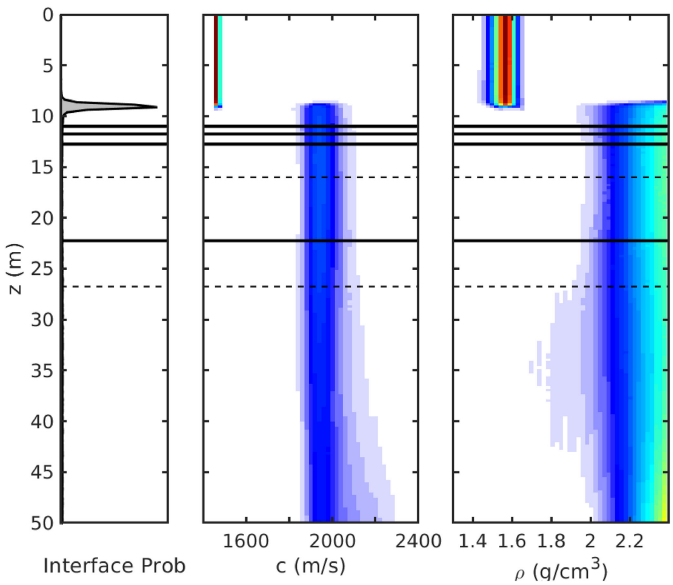

Fig. 8. Trans-D marginal posterior probability profiles for the J15 source signal. The probabilities for the geoacoustic parameter profiles are normalized globally for seabed depth from 0 to 50 m. Averaged interface depths estimated from the reflection survey are plotted as horizontal continuous black lines over the marginal probability densities. Minimum and maximum depths for the lowest horizon (deepbase2) are plotted as horizontal dashed-black lines.

impedance deep within the mud, at the specific depth where the CSS inversion shows an increase in sound speed. Putting these two results together strongly suggests that the top of the mud layer is homogeneous, but that a transition exists before the mudbase.

As done for the CSS study, inversion convergence and residual statistics have been studied. Results are similar to those of the CSS, and are not presented here.

VII. Discussion

Another important verification after inversion is to visually assess the quality of the fit between data and replicas. The estimated and predicted dispersion curves, both for CSS and J15, are presented in Fig. 9. One can see an excellent match for the two data sets.

Fig. 9 also illustrates the difference of information content between the CSS and the J15 data set. The J15 data has definitely poorer information content (fewer modes and smaller bandwidth), and so the inversion results are less informative. The higher order modes and the lower frequencies of the CSS data set allows the inversion to resolve more layers, thinner layers, and deeper layers. The downside here is the use of an impulsive and loud sound source, as opposed to the relatively quiet J15 chirp.

The trans-D result allows a statistical analysis of various seabed features. Of particular interest here is the sound-speed ratio at the mud/water interface. Its marginal posterior probability is plotted on Fig. 10, both for the chirp and for the CSS. One can note that the two distributions are virtually identical, which demonstrates inversion consistency. It also shows that the two

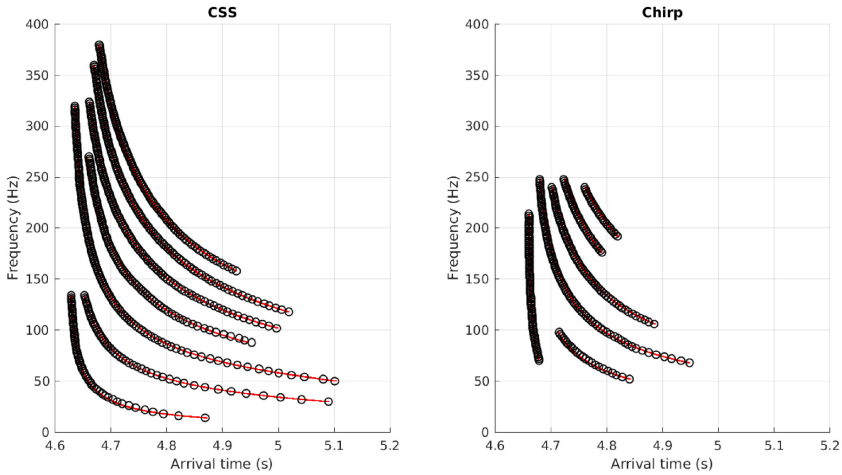

Fig. 9. Comparison between the observed dispersion curves as estimated with warping (i.e., data, black circles) and the predicted data ensembles (i.e., replicas, red lines) for the CSS (left) and J15 (right) data set. The time and frequency axis are the same for the two plots to highlight the data set differences.

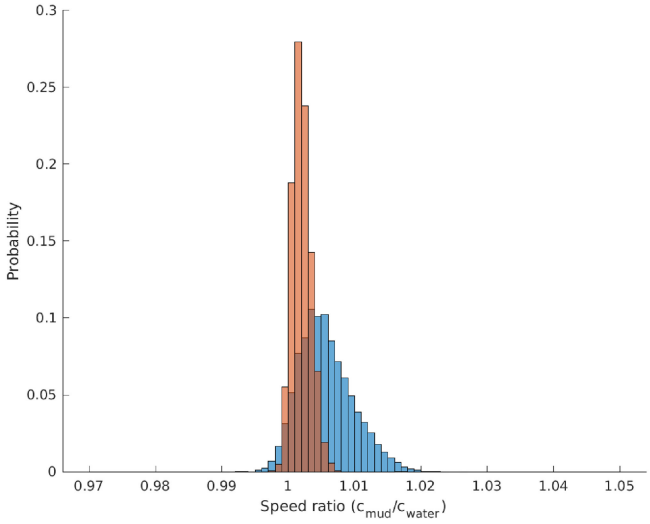

Fig. 10. Marginal posterior probability densities for the sound-speed ratio at the mud/water interface, as estimated using the CSS data (red) and the J15 data (blue).

data sets have enough information content to resolve this part of the mud. The 95% credibility interval for the sound-speed ratio is [0.9996; 1.0050] for the CSS, and [0.9989; 1.0147] for the J15. It is safe to say that the sound-speed ratio is very close to 1.

The trans-D result also shows the first $\simeq$8 m of the mud as homogeneous. This does not necessarily mean that the mud is homogeneous. As a matter of fact, the mud appears slightly laminated when looking at the seismic survey data [22]. Nonetheless, the information content of our data does not provide the resolution to discern such layers: at the frequencies considered in this paper, the acoustic behavior of the first $\simeq$8 m of mud is depth-independent. Acoustic data with a higher frequency content may be able to resolve layers within the mud.

Another interesting feature of our result is the apparent conflicting answers given by Figs. 5 and 8: at several depths, the 95% credibility interval of one inversion does not intersect the 95% credibility interval of the other. This is particularly true between 20 and 30 m, where the CSS inversion predicts a low speed/density layer (see Fig. 5) while the posterior uncertainties of the J15 inversion (see Fig. 8) do not suggest that such a layer is probable. Since the J15 data have lower information content, the inversion cannot resolve the deep layers seen in the CSS inversion, and thus the trans-D approach replaces this with a single layer. This single layer is well constrained and therefore has lower uncertainties. The key point here is that uncertainty and resolution are intimately related and both must be considered when comparing inversion results. Considering both resolution and uncertainty, the results of the two inversions are not inconsistent with each other. This clearly illustrates the importance of information content, and demonstrates that our CSS data are more informative than the J15 data.

The results obtained here can be compared with other results from the literature. Very few SBCEX results have been published at the time of writing this paper. However, this paper is part of a SBCEX special issue, and we suggest the curious reader to forage this issue to cross-compare results. Nonetheless, *in situ* measurements from a novel acoustics core system are reported in [43]. They show that the upper part of the mud layer has a constant sound speed, whose value is very close to the water sound speed. In places where mud was not too deep, the acoustic cores were able to sense a transition region one or two meters above the mud base. In this region, sound speed gradually increases and reaches values between 1500 and 1550 m/s. This fully supports the results we obtained with the CSS.

Another interesting comparison is with other inversion studies performed during SBCEX. As far as we know, Wan *et al.* [19] and Bonnel *et al.* [20] published the only two peer-reviewed articles on this subject at the time of writing this paper. Nonetheless, other studies have been presented during special sessions on SBCEX at recent ASA meetings, such as the work by Lin *et al.* [44] or by Knobles *et al.* [45]. All these references [19], [20], [44], [45] use different data sets, and different inversion methods. However, they have one important common feature. They all use the reflection survey layering as a prior deterministic information for the inversion. In other words, they do not invert for number of layers, nor for layer thickness. They all have common and consistent results: they estimate a strong gradient in the mud

layer, and a sound-speed ratio at the mud/water interface around 0.99. The estimated sound-speed ratio is consistent with our inversion result, with the acoustic cores discussed above [43], as well as with other independent *in situ* measurements [46]. On the other hand, the strong gradient does not seem realistic, as physical properties (e.g., porosity) of the mud are likely to be constant with depth—at least in the major (upper) part of the mud layer (e.g., [47]).

Still, inversion methods and data from these previous studies [19], [20], [44], [45] are solid, and their results should not be discarded thoughtlessly. It is too early to make a definitive answer about the true geoacoustic properties of the mud. However, the conclusions of the comparison of the various inversions cited above are as follows.

1) If one uses the subbottom layering from the reflection survey, then a strong gradient is required to reproduce any long range acoustic data [19], [20], [44], [45].
2) If one does not use the subbottom layering information from the preliminary survey, then no gradient is required to predict the acoustic field, as shown in this paper.

Doing inversion without the preliminary survey information may seem appealing, as it brings results that are more aligned with expected mud properties. However, it does require inversion for seabed layering. This in turn requires advanced—and computationally intensive—inversion algorithms. The success of this paper is partly due to the choice of a propagation track that is range independent, while the tracks considered in [19], [20], [44], and [45] were range dependent.

Another option to perform trans-D geoacoustic inversion without dealing with range dependent effects is to consider short range experimental setup. Indeed, if range is small enough, then range dependence is not an issue, and one can invert for seabed layering without prior information. This has been done by Belcourt *et al.* [48] on wide-angle seabed reflection-coefficient data, collected at two different sites on the Mud Patch. Their results are similar to those presented here: they also indicate that the upper part of the mud is homogeneous (with sound-speed ratio $\sim$1), but that sound speed increases a few meters before the mud base. It is significant to note that two studies based on different data sets, on different physical quantities (spherical-wave reflection coefficients versus modal dispersion curves), on different sediment models (viscous grain-shearing theory versus compressional-wave velocities and densities), and on different experimental setups ($r \leq 1$ km versus $r \sim 7$ km) lead to results that are so consistent with each other.

VIII. Conclusion

This paper presented single receiver geoacoustic inversion of two independent data sets recorded on reciprocal tracks during the 2017 SBCEX on the New England Mud Patch. The first data set is a CSS signal, a powerful impulsive source with a large bandwidth, but contaminated by several secondary bubble pulses. The second data set is a chirp emitted by a J15 source, with a low SNR. A careful combination of source deconvolution/phase compensation and warping allowed the resolution and estimation of 7 modes from 15 to 300 Hz for the CSS, and 6 modes from 52 to 248 Hz for the J15. The estimated modal dispersion curves served as input for a Bayesian geoacoustic inversion.

The chosen tracks for the two sound sources are range independent, so that both subbottom layering and geoacoustic parameters (sound speed and density) have been estimated from the data. This was done using a rigorous trans-D inversion method. In particular, the number of seabed layer interfaces and their depths were treated as unknown, and data error statistics were modeled as correlated Gaussian variables using a trans-D AR process. This hypothesis was verified *a posteriori*, after the inversion.

The seabed of the experimental area is known to have a first thick layer of fine grained sediment with clay, or mud. The inversion results show that this mud layer is homogeneous over most of its depth, with sound speed around 1460 m/s and density around 1.6 g/cm^3, which corresponds to a sound-speed ratio at the mud/water interface of nearly 1. The mud also includes a transition region, above the so-called mudbase, where speed increases by 50 to 100 m/s. These findings are consistent with *in situ* measurements performed during the experiment, as well as with other inversion results obtained in the area.

A novel feature of this paper is the comparison of two data sets, collocated independently both in time and space. Because source signals were different, the two data sets do not have the same information content. The trans-D Bayesian method used here allows an accurate quantification of this information content, which in turn allows accurate estimation of uncertainties.

The paper further illustrates that the data considered here do not have enough information content to resolve thin layers that were resolved by a previous seismic survey. If one is interested in predicting propagation on the mud patch at a few hundred hertz, then the results shown in this paper are perfectly suitable. On the other hand, if one is interested in learning as much as possible on the mud patch layering, including fine structure, then the data considered here are not sufficient. This would require higher frequency acoustic data capable of resolving thin layers. However, no single data set is fully informative. Future geoacoustic inversion research should consider meta-studies combining different data sets with different (and ideally complementary) information content.

Acknowledgment

The authors would like to thank D. Knobles and P. Wilson for leading SBCEX, and for providing the CSS/SWAMI data set. They would also like to thank P. Dahl and D. Dall'Osto for providing the J15/IVAR data set, and for their willingness to include more than a few chirps in their experimental plans. Last but not least, the authors thank the three anonymous reviewers. Their comments and suggestions have been very valuable.

References

[1] D. C. Twichell, C. E. McClennen, and B. Butman, "Morphology and processes associated with the accumulation of the fine-grained sediment deposit on the southern New England shelf," *J. Sedimentary Res.*, vol. 51, no. 1, pp. 269–280, 1981.

[2] M. H. Bothner, E. C. Spiker, P. P. Johnson, R. R. Rendigs, and P. J. Aruscavage, "Geochemical evidence for modern sediment accumulation on the continental shelf off southern new england," *J. Sedimentary Res.*, vol. 51, no. 1, pp. 281–292, 1981.

[3] F. B. Jensen, W. A. Kuperman, M. B. Porter, and H. Schmidt, *Computational Ocean Acoustics*, 2nd ed. New York, NY, USA: American Institute of Physics, 2011, ch. 5, pp. 337–455.

[4] S. M. Wiggins, M. A. McDonald, L. A. Munger, S. E. Moore, and J. A. Hildebrand, "Waveguide propagation allows range estimates for North Pacific right whales in the Bering Sea," *Can. Acoust.*, vol. 32, pp. 146–154, 2004.

[5] J. Bonnel, S. Dosso, and R. Chapman, "Bayesian geoacoustic inversion of single hydrophone light bulb data using warping dispersion analysis," *J. Acoust. Soc. Amer.*, vol. 134, pp. 120–130, 2013.

[6] J. Bonnel, A. M. Thode, S. B. Blackwell, K. Kim, and A. M. Macrander, "Range estimation of bowhead whale (Balaena mysticetus) calls in the arctic using a single hydrophone," *J. Acoust. Soc. Amer.*, vol. 136, no. 1, pp. 145–155, 2014.

[7] G. A. Warner, S. E. Dosso, D. E. Hannay, and J. Dettmer, "Bowhead whale localization using asynchronous hydrophones in the Chukchi sea," *J. Acoust. Soc. Amer.*, vol. 140, no. 1, pp. 20–34, 2016.

[8] M. S. Ballard, G. V. Frisk, and K. M. Becker, "Estimates of the temporal and spatial variability of ocean sound speed on the New Jersey shelf," *J. Acoust. Soc. Amer.*, vol. 135, no. 6, pp. 3316–3326, 2014.

[9] G. A. Warner, S. E. Dosso, J. Dettmer, and D. E. Hannay, "Bayesian environmental inversion of airgun modal dispersion using a single hydrophone in the Chukchi sea," *J. Acoust. Soc. Amer.*, vol. 137, no. 4, pp. 2361–2362, 2015.

[10] G. R. Potty, J. H. Miller, J. F. Lynch, and K. B. Smith, "Tomographic inversion for sediment parameters in shallow water," *J. Acoust. Soc. Amer.*, vol. 108, pp. 973–986, 2000.

[11] P. S. Petrov, "A method for single-hydrophone geoacoustic inversion based on the modal group velocities estimation: Application to a waveguide with inhomogeneous bottom relief," in *Proc. Days Diffraction*, 2014, pp. 186–191.

[12] L. Wan, M. Badiey, and D. P. Knobles, "Geoacoustic inversion using low frequency broadband acoustic measurements from l-shaped arrays in the shallow water 2006 experiment," *J. Acoust. Soc. Amer.*, vol. 140, no. 4, pp. 2358–2373, 2016.

[13] J. Bonnel, C. Gervaise, P. Roux, B. Nicolas, and J. I. Mars, "Modal depth function estimation using time-frequency analysis," *J. Acoust. Soc. Amer.*, vol. 130, pp. 61–71, 2011.

[14] G. Le Touzé, B. Nicolas, J. Mars, and J. L. Lacoume, "Matched representations and filters for guided waves," *IEEE Trans. Signal Process.*, vol. 57, no. 5, pp. 1783–1795, May 2009.

[15] J. Bonnel, C. Gervaise, B. Nicolas, and J. I. Mars, "Single-receiver geoacoustic inversion using modal reversal," *J. Acoust. Soc. Amer.*, vol. 131, no. 1, pp. 119–128, 2012.

[16] A. Thode *et al.*, "Using nonlinear time warping to estimate north pacific right whale calling depths in the Bering sea," *J. Acoust. Soc. Amer.*, vol. 141, no. 5, pp. 3059–3069, 2017.

[17] Y. B. Qi, S. H. Zhou, R. H. Zhang, and Y. Ren, "A waveguide-invariant-based warping operator and its application to passive source range estimation," *J. Comput. Acoust.*, vol. 23, no. 1, 2015, Art. no. 1550003.

[18] H. Niu, R. Zhang, and Z. Li, "Theoretical analysis of warping operators for non-ideal shallow water waveguides," *J. Acoust. Soc. Amer.*, vol. 136, no. 1, pp. 53–65, 2014.

[19] L. Wan, M. Badiey, D. P. Knobles, and P. S. Wilson, "The airy phase of explosive sounds in shallow water," *J. Acoust. Soc. Amer.*, vol. 143, no. 3, pp. EL199–EL205, 2018.

[20] J. Bonnel *et al.*, "Geoacoustic inversion on the new england mud patch using warping and dispersion curves of high-order modes," *J. Acoust. Soc. Amer.*, vol. 143, no. 5, pp. EL405–EL411, 2018.

[21] A. R. McNeese, J. D. Sagers, P. S. Wilson, and D. P. Knobles, "An investigation of the combustive sound source," in *Proc. Meetings Acoust.*, 2010, vol. 9, Paper 005002.

[22] J. Goff, J. D. Chaytor, A. H. Reed, S. Liu, P. S. Wilson, and D. P. Knobles, "The coarse-to fine-grained boundary beneath the new england mud patch: Evidence from seismic and core data for an abrupt post-transgressive change in hydrologic regime on the continental shelf," in *Proc. AGU Fall Meeting Abstr.*, 2016.

[23] J. Bonnel, G. Le Touzé, B. Nicolas, and J. Mars, "Physics-based time-frequency representations for underwater acoustics: Power class utilization with waveguide-invariant approximation," *IEEE Signal Process. Mag.*, vol. 30, no. 6, pp. 120–129, Nov. 2013.

[24] R. W. Clayton and R. A. Wiggins, "Source shape estimation and deconvolution of teleseismic bodywaves," *Geophys. J. Int.*, vol. 47, no. 1, pp. 151–177, 1976.

[25] R. G. Baraniuk and D. L. Jones, "Unitary equivalence: A new twist on signal processing," *IEEE Trans. Signal Process.*, vol. 43, no. 10, pp. 2269–2282, Oct. 1995.

[26] S. N. Sergeev *et al.*, "Separation of acoustic modes in the Florida straits using noise interferometry," *Acoust. Phys.*, vol. 63, no. 1, pp. 76–85, 2017.

[27] X.-D. Zhang, L.-X. Wu, H.-Q. Niu, and R.-H. Zhang, "Sequential parameter estimation using modal dispersion curves in shallow water," *Chin. Phys. Lett.*, vol. 35, no. 4, 2018, Art. no. 044301.

[28] J. Bonnel, S. Caporale, and A. Thode, "Waveguide mode amplitude estimation using warping and phase compensation," *J. Acoust. Soc. Amer.*, vol. 141, no. 3, pp. 2243–2255, 2017.

[29] P. J. Green, "Reversible jump Markov chain Monte Carlo computation and Bayesian model determination," *Biometrika*, vol. 82, no. 4, pp. 711–732, 1995.

[30] J. Dettmer, S. E. Dosso, and C. W. Holland, "Trans-dimensional geoacoustic inversion," *J. Acoust. Soc. Amer.*, vol. 128, no. 6, pp. 3393–3405, 2010.

[31] A. Malinverno, "Parsimonious Bayesian Markov chain Monte Carlo inversion in a nonlinear geophysical problem," *Geophys. J. Int.*, vol. 151, no. 3, pp. 675–688, 2002.

[32] S. E. Dosso, J. Dettmer, G. Steininger, and C. W. Holland, "Efficient trans-dimensional Bayesian inversion for geoacoustic profile estimation," *Inverse Problems*, vol. 30, no. 11, 2014, Art. no. 114018.

[33] S. E. Dosso and M. J. Wilmut, "Uncertainty estimation in simultaneous Bayesian tracking and environmental inversion," *J. Acoust. Soc. Amer.*, vol. 124, pp. 82–97, 2008.

[34] D. J. Earl and M. W. Deem, "Parallel tempering: Theory, applications, and new perspectives," *Phys. Chem. Chem. Phys.*, vol. 7, no. 23, pp. 3910–3916, 2005.

[35] M. Sambridge, "A parallel tempering algorithm for probabilistic sampling and multimodal optimization," *Geophys. J. Int.*, vol. 196, no. 1, pp. 357–374, 2014.

[36] E. Xiang, R. Guo, S. E. Dosso, J. Liu, H. Dong, and Z. Ren, "Efficient hierarchical trans-dimensional Bayesian inversion of magnetotelluric data," *Geophys. J. Int.*, vol. 213, no. 3, pp. 1751–1767, 2018.

[37] J. Dettmer and S. E. Dosso, "Trans-dimensional matched-field geoacoustic inversion with hierarchical error models and interacting Markov chains," *J. Acoust. Soc. Amer.*, vol. 132, no. 4, pp. 2239–2250, 2012.

[38] G. Steininger, J. Dettmer, S. E. Dosso, and C. W. Holland, "Trans-dimensional joint inversion of seabed scattering and reflection data," *J. Acoust. Soc. Amer.*, vol. 133, no. 3, pp. 1347–1357, 2013.

[39] C. F. Mecklenbräuker and P. Gerstoft, "Objective functions for ocean acoustic inversion derived by likelihood methods," *J. Comput. Acoust.*, vol. 8, no. 2, pp. 259–270, 2000.

[40] S. E. Dosso and M. J. Wilmut, "Data uncertainty estimation in matched-field geoacoustic inversion," *IEEE J. Ocean. Eng.*, vol. 31, no. 2, pp. 470–479, Apr. 2006.

[41] E. K. Westwood, C. T. Tindle, and N. R. Chapman, "A normal mode model for acousto-elastic ocean environments," *J. Acoust. Soc. Amer.*, vol. 100, no. 6, pp. 3631–3645, 1996.

[42] E. L. Hamilton, "Geoacoustic modeling of the sea floor," *J. Acoust. Soc. Amer.*, vol. 68, pp. 1313, 1980.

[43] M. S. Ballard, K. M. Lee, A. R. McNeese, P. S. Wilson, and J. A. Goff, "Development of a system for in situ measurements of geoacoustic properties during sediment coring," in *Proc. Meetings Acoust.*, 2016, vol. 26, Paper 070001.

[44] Y.-T. Lin, T. F. Duda, A. Newhall, and G. Gawarkiewicz, "Surface wave effects on bottom geoacoustic inversions," *J. Acoust. Soc. Amer.*, vol. 142, no. 4, pp. 2590–2590, 2017.

[45] D. P. Knobles, P. S. Wilson, W. S. Hodgkiss, L. Wan, and M. Badiey, "Bayesian-maximum entropy method applied to seabed geoacoustic models using broadband and narrowband acoustic measurements," *J. Acoust. Soc. Amer.*, vol. 142, no. 4, pp. 2557–2557, 2017.

[46] J. Yang, "In situ measurements of sediment sound speed and attenuation at the seabed characterization experiment site in the frequency band of 0.5–10 kHz," *J. Acoust. Soc. Amer.*, vol. 142, no. 4, pp. 2589–2589, 2017.

[47] J. Chaytor, B. Buczkowksi, A. Paquette, J. Goff, A. Reed, and E. Sweeney, "NE mud patch core status and sediment analyse (EN577 Legs 1 and 2 cores)," in *Proc. ONR SBCEX Workshop*, 2017.

[48] J. Belcourt, S. E. Dosso, C. W. Holland, and J. Dettmer, "Bayesian geoacoustic inversion of seabed reflection data at the new england mud patch," *J. Acoust. Soc. Amer.*, vol. 142, no. 4, pp. 2590–2590, 2017.

Julien Bonnel (S'08–M'11) received the Ph.D. degree in signal processing from Grenoble Institut National Polytechnique, Grenoble, France, in 2010.

From 2010 to 2017, he was an Assistant Professor with Lab-STICC (UMR 6285), ENSTA Bretagne, Brest, France. Since September 2017, he has been an Associate Scientist with Woods Hole Oceanographic Institution, Woods Hole, MA, USA. His research in signal processing and underwater acoustics include time-frequency analysis, source detection/localization, geoacoustic inversion, acoustical tomography, passive acoustic monitoring, and bioacoustics.

Stan E. Dosso received the B.Sc. and M.Sc. degrees in physics and applied mathematics from the University of Victoria, Victoria, BC, Canada, in 1982 to 1985, and the Ph.D. degree in geophysics from The University of British Columbia, Vancouver, BC, Canada, in 1990.

He worked with the Defence Research Establishment Pacific, Victoria, BC, Canada, from 1990–1995, before taking up an Ocean Acoustics Research Chair with the School of Earth and Ocean Sciences, University of Victoria, where he is currently a Professor and the Director of the School. He has authored or coauthored more than 155 papers in peer-reviewed journals. His research interests involve inverse problems in ocean acoustics (seabed geoacoustics and source localization) and geophysics (earthquake seismology and geoelectromagnetism). His focus in all areas is the development and application of Bayesian (probabilistic) inversion methods which provide quantitative uncertainty analyses that yield insight into the properties/processes under investigation.

Dr. Stan is a Fellow of the Acoustical Society of America and a member of the Canadian Acoustical Association, which he served as a President from 2003–2007. He is an Associate Editor of the *Journal of the Acoustical Society of America*, and has served as a Conference Chair for an ASA meeting and three CAA meetings. He was the recipient of the ASA Medwin Prize in acoustical oceanography and the Science Teaching Excellence Award by the University of Victoria.

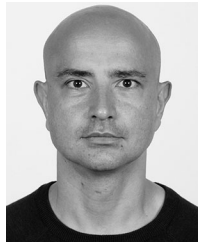

Dimitrios Eleftherakis received the Graduate degree in mechanical engineering from the University of Patras, Patras, Greece, in 1998, the M.Sc. degree in offshore and ocean technology (specialization: diving and underwater technology), Cranfield University, Cranfield, U.K., in 2005–2006, and the Ph.D. degree from TU Delft, Delft, The Netherlands, in 2009–2013, where he developed methods for classifying sediments on Dutch riverbeds using multibeam echosounder (MBES) data.

From 2015 to 2018, he worked as a Postdoctoral Researcher in France, first at Ifremer (MBES backscatter calibration) and then at ENSTA-Bretagne (geoacoustic inversion).

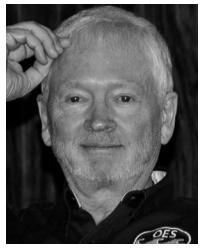

N. Ross Chapman (M'97–SM'03–F'10) received the Ph.D. degree in physics from the University of British Columbia, Vancouver, BC, Canada, in 1975.

He was the Leader of the Ocean Acoustics Group with the Defence Research in Canada (1976–1995), before moving on to the University of Victoria as a Research Chair in Ocean Acoustics, and the Director of the Centre for Earth and Ocean Sciences with the University of Victoria (2000–2006). He recently retired from the University of Victoria following a career of more than 35 years in underwater acoustics, signal processing, and acoustical oceanography. He has authored or coauthored more than 130 papers and book chapters, and continues to maintain his research interests in ocean acoustic propagation and modeling, advanced signal processing, ocean ambient noise measurement and modeling, and inversion of ocean seabed properties from acoustic field data.

Dr. Chapman is fellow of the two societies, and served as an Editor-in-Chief for the IEEE JOURNAL OF OCEANIC ENGINEERING from 2012 to 2017.